Zintl chemistry leading to ultralow thermal conductivity, semiconducting behavior, and high thermoelectric performance of hexagonal KBaBi

Zhenzhen Feng,[1,2] Yuhao Fu,[3] Yuli Yan,[1,*] Yongsheng Zhang,[4,5,†] and David J. Singh[2,6,‡]

[1]*Institute for Computational Materials Science, School of Physics and Electronics, Henan University, Kaifeng 475004, China*

[2]*Department of Physics and Astronomy, University of Missouri, Columbia, Missouri 65211, USA*

[3]*College of Physics, Jilin University, Changchun 130012, China*

[4]*Key Laboratory of Materials Physics, Institute of Solid State Physics, Chinese Academy of Sciences, Hefei 230031, China*

[5]*Science Island Branch of Graduate School, University of Science and Technology of China, Hefei 230026, China*

[6]*Department of Chemistry, University of Missouri, Columbia, Missouri 65211, USA*

(Received 8 February 2021; revised 26 April 2021; accepted 19 May 2021; published 1 June 2021)

We identify the ground state structure of the phase KBaBi using *ab initio* evolutionary structure search methods and demonstrate that the bonding of this compound leads to a combination of very low thermal conductivity and electronic properties that are favorable for thermoelectric performance. The structure is the hexagonal ZrBeSi-type structure, with the cubic half-Heusler structure as a higher-energy competing phase. The bonding of the hexagonal structure leads to strongly anharmonic vibrational properties, which underlie the low thermal conductivity. The calculated figure of merit is approximately $ZT = 3$ at 1000 K with optimized doping. This work underscores the use of chemical control of bonding to obtain low thermal conductivity and identifies a chemistry that achieves this.

DOI: 10.1103/PhysRevB.103.224101

I. INTRODUCTION

Thermoelectric (TE) materials are a subject of considerable recent interest. The reason is their potential applications in energy technology [1–4] and the exciting scientific challenges posed by the need to resolve contradictory electrical and thermal transport requirements for high thermoelectric performance [5–7]. The conversion efficiency of a TE device is limited by the thermoelectric figure of merit $ZT = \sigma S^2 T/(\kappa_e + \kappa_l)$ of the semiconductor materials used in it. Here S is the Seebeck coefficient, σ is the electrical conductivity, κ_e is the electronic thermal conductivity, κ_l is the lattice thermal conductivity, and T is the absolute temperature [8]. For example, a high power factor, $PF = S^2\sigma$, in the numerator of ZT requires a high Seebeck coefficient, generally a characteristic of heavy-mass semiconductors at low doping levels and, at the same time, high conductivity, generally occurring in light-mass semiconductors and at heavy doping. Low thermal conductivity, needed for high ZT, generally requires soft anharmonic lattices, as in ionic crystals, and strong phonon scattering, while high electrical conductivity is characteristic of semiconductors with stiff covalent bonding and low scattering, as in silicon and GaAs.

These contradictions have led to a variety of approaches for overcoming them. They have been of importance beyond the field of thermoelectrics, for example, through better understanding of the role of band structure and its engineering, nanostructure to modify thermal and electronic transport [9–11], theoretical methods for thermal conductivity [12], and improved understanding of the interplay of chemical bonding and transport in complex semiconductors [13–15]. Exploration of novel chemistries is an important way forward in developing this understanding.

Here we extend this by showing a chemistry for simultaneously obtaining ultralow thermal conductivity and favorable electronic transport. This is achieved in hexagonal KBaBi, which we identify as a stable compound based on first-principles evolutionary structure search. This compound is based on the Zintl concept, where the electropositive K provide electrons to a layered semiconducting Ba-Bi framework based on nominal Bi^{3-}. This anionic framework structure leads to soft phonons, large anharmonicity, and low thermal conductivity while maintaining dispersive bands that favor electrical conductivity.

KBaBi is a composition that was identified as a possible cubic half-Heusler structure compound [16]. In particular, it shows thermodynamic stability with respect to known competing phases and does have stable phonons in the half-Heusler structure. While this thermodynamic stability does imply that KBaBi is likely a stable phase, it does not prove that it will occur with the half-Heusler structure as there may be other lower-energy structures. It is interesting though that it would have low thermal conductivity in the half-Heusler structure [16,17]. Furthermore, the half-Heuslers are a family of compounds that contain many excellent thermoelectric materials, are cubic, and typically exhibit other properties, particularly mechanical properties, and stability that favor applications [18–20]. Thus, KBaBi would be a very interesting thermoelectric composition in the half-Heusler structure.

We note that the half-Heusler structure is a broad family of compounds with diverse chemistry. However, the

*yanyl@henu.edu.cn
†yshzhang@theory.issp.ac.cn
‡singhdj@missouri.edu

combination of two very electropositive elements with Bi is unusual, suggesting that the structure may be different, as has also been noted in other prospective half-Heusler compounds. For instance, LiZnSb and LiAlSi adopt, instead, hexagonal structures [21,22], while HfCoAs, VCoGe, NbFeAs, and NiTiGe are orthorhombic [23,24].

Alternately, Zhang and coworkers, also based on thermodynamic stability against competing phases, predicted that KBaBi is stable in the hexagonal ZrBeSi-type structure and that it would be a topological insulator in that structure due to a band inversion at the zone center [25]. Subsequent theoretical work indicated that the electrical and thermal transport properties of this hexagonal phase are consistent with good thermoelectric performance [26,27]. Thus, Carrete and coworkers [16] and Zhang and coworkers [25] found that KBaBi is likely a stable phase, but using different hypothesized crystal structures. To the best of our knowledge neither the half-Heusler nor the hexagonal structures of KBaBi have been reported experimentally.

As usual, one may expect a strong interplay between crystal structure, bonding, and properties. This necessitates determination of the structure in order to properly elucidate the thermoelectric and other properties.

II. STRUCTURE DETERMINATION

The chemical bonding of a material is intimately connected to the crystal structure, and transport properties in turn are controlled by the structure and bonding. We used the unbiased particle swarm structure search method as implemented in the CALYPSO code [28,29] to determine the stable crystal structure. The global optimization was done for the total energy as determined within density functional theory (DFT). We used the Perdew-Burke-Ernzerhof generalized gradient approximation (PBE-GGA) [30]. The energies of optimized structures were determined using the projector augmented wave method [31], as implemented in the Vienna Ab initio Simulation Package (VASP) [32]. Good convergence is obtained with an energy cutoff of 400 eV for the plane-wave expansion and a $2\pi \times 0.03$ Å^{-1} **k**-point mesh in the Brillouin zone, which were the parameters used. The criterion of the energy convergence for the self-consistent cycles was 10^{-8} eV, and the forces on individual atoms in relaxations were less than 10^{-4} eV/Å. We used a higher cutoff of 600 eV for the two final total energy calculations. We searched for possible KBaBi structures including unit cells up to 12 atoms (4 f.u.). The evolutionary search was done for 50 generations, with each generation containing 50 structures. The lowest structure was found to have 2 f.u./cell. As seen in Fig. 1, no new ground states were identified in the final generations, which is characteristic of completion of the global optimization.

The lowest-energy structure found was a hexagonal ($P6_3/mmc$) structure, as shown in Fig. 2(a). The previously studied cubic phase ($F\bar{4}3m$) is also a low-energy structure and is shown in Fig. 2(b). These are the ZrBeSi-type structure and the half-Heusler structure, which, as mentioned, are both suggested structures based on stability against known competing phases [16,25]. The hexagonal structure is based on honeycomb lattice layers of alternating Ba and Bi and is centrosymmetric, while the cubic structure is

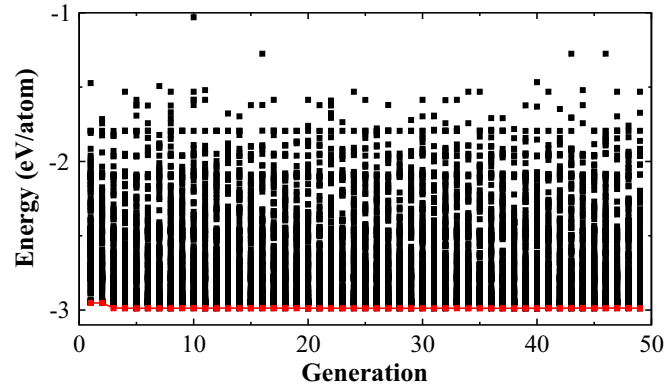

FIG. 1. Energies of structures in different generations as obtained in the global optimization search for the ground state of KBaBi. The red line connects the lowest-energy structures in different generations.

noncentrosymmetric. In between these in energy are three other structures, with space groups $Imm2$ (30 meV/atom above the ground state), $R\bar{3}m$ (34 meV/atom above the ground state), and Pm (36 meV/atom above the ground state). The $R\bar{3}m$ structure, however, shows phonon instabilities and is therefore not a viable phase. In the following we focus on the ground state $P6_3/mmc$ in comparison with the previously suggested half-Heusler ($F\bar{4}3m$) structure, which is 40 meV/atom above the ground state.

Figures 2(c) and 2(d) show the calculated electron localization function (ELF) for the two structures [33]. The energy difference between these is approximately 40 meV per atom. This is above the normal range of DFT errors for the energy

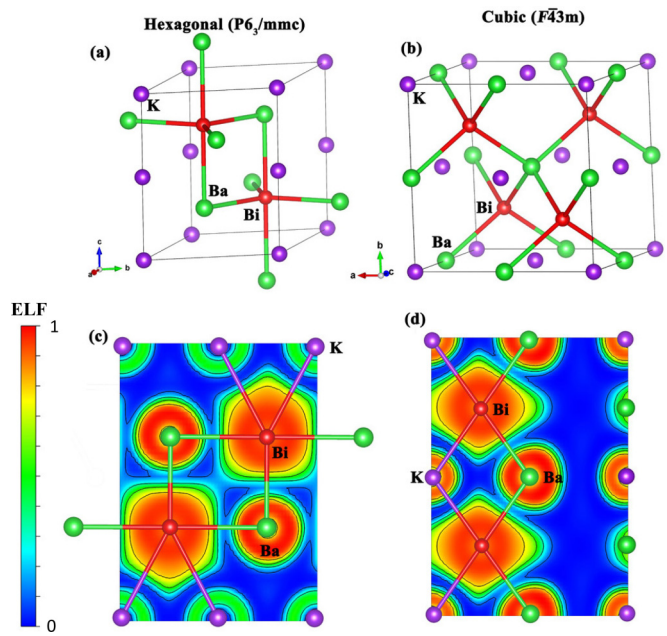

FIG. 2. (a) The lowest-energy structure of KBaBi, space group $P6_3/mmc$. (b) Crystal structure of the half-Heusler structure of KBaBi. Electron localization function (ELF) for the (c) hexagonal and (d) cubic phases of KBaBi. The scale bar for the ELF is shown on the left.

differences between phases. The hexagonal structure is lowest in energy, and therefore, it and not the half-Heusler structure is the predicted ground state. As discussed below, we also calculated the temperature-dependent Gibbs free-energy difference between these two phases at zero pressure using the phonon dispersions as well as the pressure dependence of the energy difference. The ground state hexagonal phase is further stabilized relative to the cubic by temperature due to its softer bonding. In addition the cubic phase cannot be stabilized by moderate pressure.

The calculated lattice constants of the ground state hexagonal $P6_3/mmc$ structure are $a = 6.19$ Å, $c = 7.61$ Å, with all atoms on symmetry sites: K at (0, 0, 0), Ba at (1/3, 2/3, 1/4), and Bi at (2/3, 1/3, 1/4). Ba and Bi are coplanar, forming anionic $(BaBi)^-$ sheets. The layer stacking forms -Bi-Ba-Bi-Ba- chains along the c axis. The K cations are between these sheets, providing charge balance and stabilizing the layered structure. Each Bi is coordinated by three Ba atoms in the layer, with bond length 3.57 Å, and two Ba, one above and one below, in the chains, at a significantly longer distance of 3.81 Å. The Bi-K distance is 4.05 Å. This is considerably different from the half-Heusler structure, where Bi and Ba form a tetrahedral framework with a bond length of 3.65 Å and the K fill octahedral sites around the Ba atom, leading to the same tetrahedral coordinated Bi-K bond length of 3.65 Å. Thus, the coordination of the nominal Bi^{3-} anions is by four Ba^{2+} and four K^+, both at 3.65 Å, in the half-Heusler structure and by three Ba^{2+} at 3.57 Å and another two Ba^{2+} at 3.81 Å, plus six K^+ at 4.05 Å, in the hexagonal structure. In this sense, the hexagonal structure is a more ionic structure in having higher coordination of anions by cations along with generally longer bond lengths, differentiated to bring the higher charged cations closer relative to the lower charged cations. This suggests a softer and more anharmonic lattice with the potential for lower thermal conductivity, as we find below. It should be noted that this is related to packing and not a consequence of a lower density in the hexagonal phase since the hexagonal phase has a higher density. The cubic structure has a primitive unit cell with 1 f.u. and a volume of 149.6 $Å^3$, while the hexagonal structure has a unit cell with 2 f.u. and a volume of 253.1 $Å^3$.

The ELF can be expressed as $\mathrm{ELF}(\mathbf{r}) = (1 + \{K(\mathbf{r})/K_h[\rho(\mathbf{r})]\}^2)^{-1}$, where K is the curvature of the electron pair density for electrons of identical spin, $\rho(\mathbf{r})$ is the density at $\mathbf{r}$, and $K_h[\rho(\mathbf{r})]$ is the value of K in a homogeneous electron gas with density ρ. The ELF may be used to characterize the degree of electron localization to identify the character of chemical bonding. The ELF lies between 0 and 1. An ELF of 0 corresponds to no localization as in regions with no electrons. A value of 0.5 reflects the behavior of a homogeneous electron gas, with values near 0.5 being characteristic of metallic bonding. An ELF value of 1 indicates full localization, with high values characterizing covalent bonds, core shells, and lone pairs. While descriptions of bonding in real materials are necessarily qualitative, the ELF can be useful in characterizing differences in bonding between compounds [33].

As seen in the ELF and also in the electronic density of states (DOS) discussed below, both the cubic and hexagonal structures show ionic bonding for K and Ba, which is as expected from the strongly electropositive nature of these atoms. There is some rather weak, but still discernible, covalency seen in both structures based on the slightly higher ELF in the region between these atoms relative to the quite low values in the interstitial. Still, the ELF values in the area between Bi and Ba are low in both compounds, amounting to 0.12 and 0.15 for the hexagonal and cubic structures, respectively. These are as measured in the ab plane for the cubic structure and along the c direction for the hexagonal structure. Thus, these compounds are basically ionic with some weak covalency. Having obtained the predicted ground state and first metastable structures, we proceed to analyze the properties.

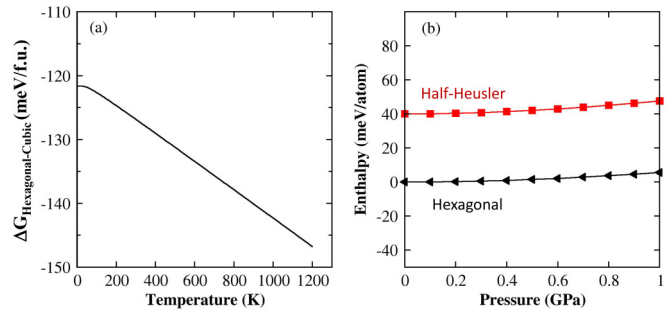

FIG. 3. (a) Temperature-dependent free-energy difference between the hexagonal and cubic structures. (b) Pressure-dependent enthalpy relative to the zero-pressure ground state.

III. PHONONS AND THERMAL CONDUCTIVITY

We calculated the vibrational properties for both the ground state hexagonal and cubic phases. The harmonic second-order interatomic force constants (IFCs) and phonon dispersions were obtained using the frozen phonon method implemented in the PHONOPY package [34]. We used a $3 \times 3 \times 3$ supercell containing 162 atoms for the hexagonal phase and a $4 \times 4 \times 4$ supercell containing 192 atoms for the cubic structure for this purpose.

The calculated phonon dispersions for the two structures are compared in Fig. 4. The corresponding Grüneisen parameters γ are indicated on the phonon dispersions. We calculated the vibrational contributions to the Gibbs free energy G and entropy S, which can be written as $G = E + H_{\mathrm{vib}} - TS_{\mathrm{conf}} - TS_{\mathrm{vib}}$, where E is the DFT-calculated total energy, H_{vib} is the vibrational enthalpy, and S_{conf} and S_{vib} are the configurational and vibrational entropies, respectively. The free-energy difference of two phases is defined as $\Delta G = \Delta E + \Delta H_{\mathrm{vib}} - T\Delta S_{\mathrm{conf}} - T\Delta S_{\mathrm{vib}}$; ΔS_{conf} is zero for pristine material. The temperature dependence of the free-energy difference including the vibrational entropy is shown in Fig. 3(a). As mentioned above, the hexagonal structure remains stable over the cubic structure independent of temperature.

Returning to the phonons, the acoustic frequencies are lower in hexagonal KBaBi than in cubic KBaBi, which means that hexagonal KBaBi has lower acoustic phonon velocities. This favors lower thermal conductivity. There are other important differences, particularly a peak in the phonon density of states (PHDOS) of the hexagonal structure starting

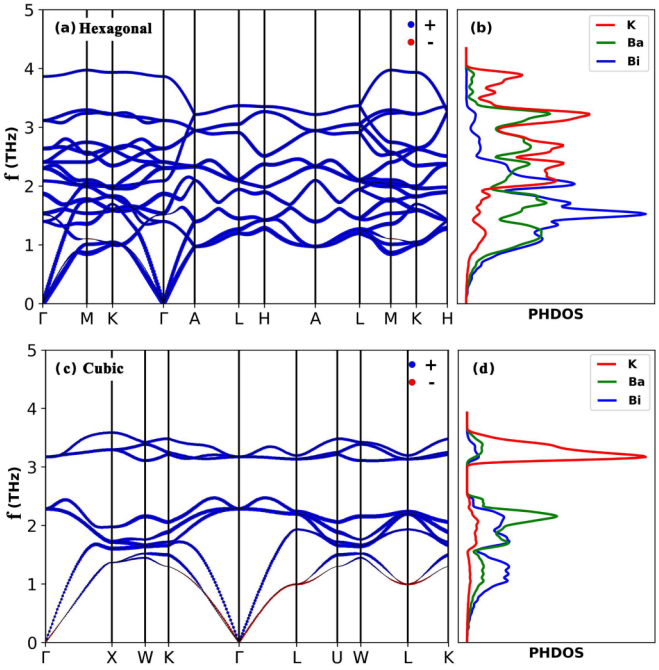

FIG. 4. Calculated phonon dispersion curves for (a) hexagonal and (c) cubic phases of KBaBi. The symbol sizes give the Grüneisen parameters γ of each phonon mode. Blue (+) and red (−) indicate positive and negative γ, respectively. The (projected) phonon density of states (PHDOS) for (b) hexagonal and (d) cubic structures.

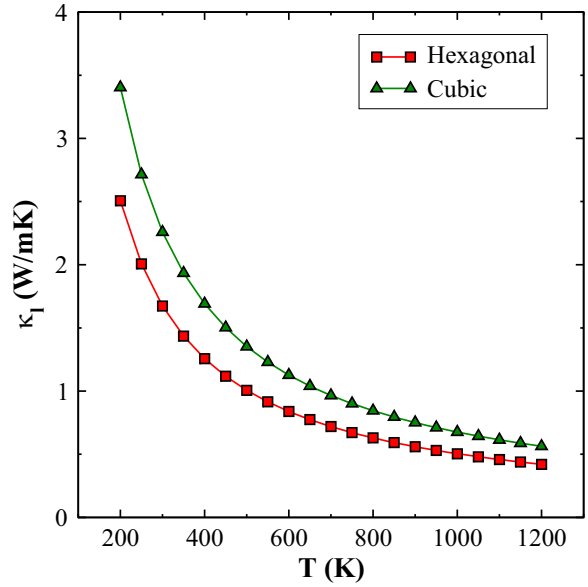

FIG. 5. Calculated temperature-dependent lattice thermal conductivity for the hexagonal and cubic structures of KBaBi.

at ∼1 THz and extending up to ∼2 THz of Bi character with two subpeaks of Ba character in this frequency range. This arises from flat branches in the dispersion. The cubic structure also shows peaks in the PHDOS, but these are less pronounced, reflecting more dispersive optical branches. Interactions between low-frequency optical phonons and the acoustic branches can lead to enhanced scattering of the heat-carrying acoustic phonons. This again suggests the possibility of lower lattice thermal conductivity in hexagonal KBaBi. Large-magnitude Grüneisen parameters indicate strong anharmonicity and hence a low thermal conductivity. As shown in Fig. 4, hexagonal KBaBi has larger Grüneisen parameters for the acoustic branches than found in the cubic structure. This again suggests low thermal conductivity for the hexagonal structure since acoustic branches generally play an important role in heat conduction. This expectation is confirmed by detailed thermal conductivity calculations.

The lattice thermal conductivity κ_l at temperature T can be calculated via the linearized Boltzmann transport equation [35] as the sum of contributions over all the phonon modes λ with branch p and wave vector $\mathbf{q}$:

$$\kappa_l \equiv \kappa_{\alpha\alpha} = \frac{1}{NV}\sum_{\lambda}\frac{\partial f}{\partial T}(\hbar\omega_\lambda)v_\lambda^\alpha v_\lambda^\alpha \tau_\lambda. \tag{1}$$

The phonon lifetime τ_λ is controlled by two processes: two-phonon scattering from isotopic disorder and three-phonon anharmonic scattering, which is a sum of the two-phonon isotopic scattering rate $1/\tau^{\rm iso}$ and the three-phonon anharmonic scattering rate $1/\tau^{\rm anh}$. Here $1/\tau^{\rm anh}$ can be determined as the sum over three-phonon transition probabilities $\Gamma^{\pm}_{\lambda\lambda'\lambda''}$, which are calculated as

$$\Gamma^{\pm}_{\lambda\lambda'\lambda''} = \frac{\hbar\pi}{8N}\begin{Bmatrix}2(f_{\lambda'}-f_{\lambda''})\\ f_{\lambda'}+f_{\lambda''}+1\end{Bmatrix}\frac{\delta(\omega_\lambda \pm \omega_{\lambda'}-\omega_{\lambda''})}{\omega_\lambda\omega_{\lambda'}\omega_{\lambda''}}|V^{\pm}_{\lambda\lambda'\lambda''}|^2, \tag{2}$$

where the upper (lower) row in the curly brackets corresponds to the + (−) sign denoting absorption (emission) processes. The three-phonon scattering phase space $W^{\pm}_{\lambda}$ is defined as the sum of frequency-containing factors in the expression for $\Gamma^{\pm}_{\lambda\lambda'\lambda''}$ and is [36–38]

$$W^{\pm}_{\lambda} = \frac{1}{2N}\sum_{\lambda' p''}\begin{Bmatrix}2(f_{\lambda'}-f_{\lambda''})\\ f_{\lambda'}+f_{\lambda''}+1\end{Bmatrix}\frac{\delta(\omega_\lambda \pm \omega_{\lambda'}-\omega_{\lambda''})}{\omega_\lambda\omega_{\lambda'}\omega_{\lambda''}} \tag{3}$$

for absorption (+) and emission (−) processes.

The third-order IFCs, needed for the thermal conductivity, were calculated using real-space supercells via the SHENGBTE package [35]. For this purpose we imposed a cutoff of 5.0 Å for the interaction range. Convergence tests were done for the cutoff range. We find that a cutoff of 4 Å would be inadequate, while 6 Å would yield somewhat lower thermal conductivities than 5 Å, which would lead to slightly higher predictions for ZT. The lattice thermal conductivities κ_l were calculated by iteratively solving the linearized Boltzmann-Peierls transport equation for phonons as implemented in the SHENGBTE package. A phonon momentum $\mathbf{q}$ mesh of 15 × 15 × 15 was used in solving the transport equation.

The temperature-dependent lattice thermal conductivities κ_l of the two structures are shown in Fig. 5. As seen, κ_l of the hexagonal ground state structure is much lower than for the half-Heusler. Near room temperature, κ_l are 1.67 and 2.26 W/mK for hexagonal and cubic structures, respectively. This value for the hexagonal phase is somewhat lower than the value reported by Barman and coworkers based on the Boltzmann transport equation for phonons [27]. As mentioned, the low values of κ_l for the hexagonal structure can be anticipated in terms of the bonding and phonons. This is reflected in

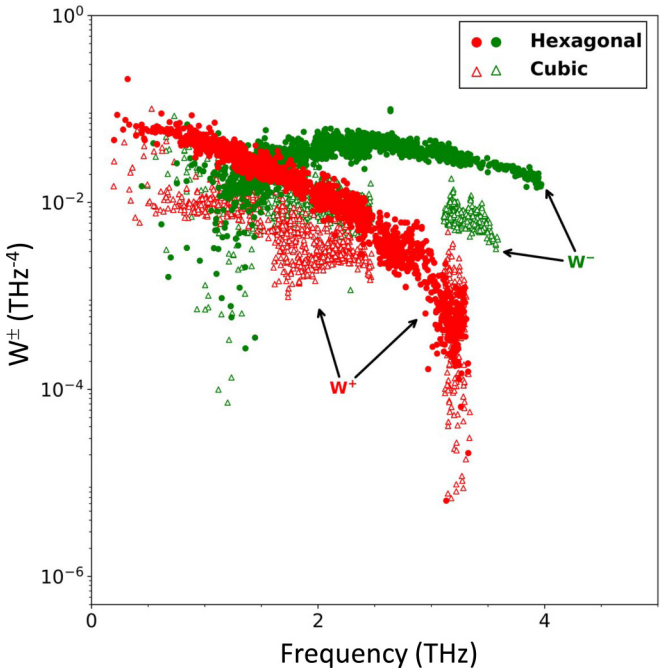

FIG. 6. Calculated scattering phase space for phonon modes in hexagonal and cubic structures of KBaBi. The + (−) sign denotes three-phonon absorption (emission). Note the logarithmic scale.

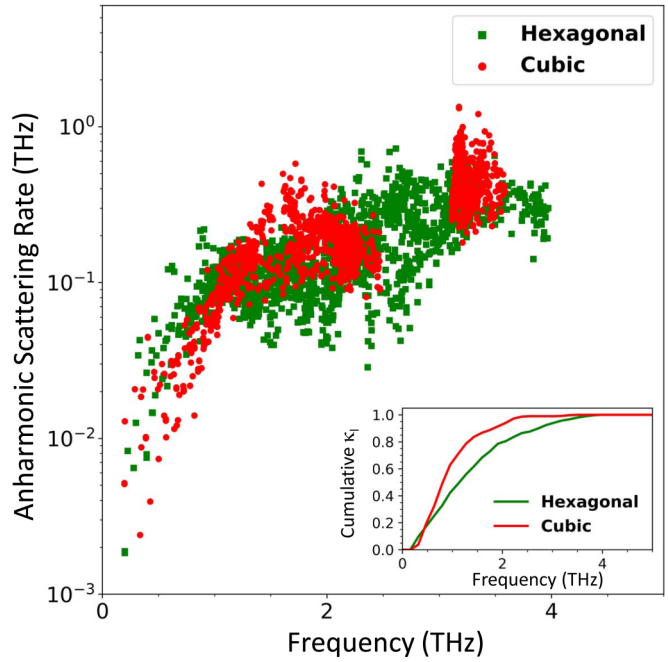

FIG. 7. Calculated anharmonic scattering rates at 300 K. The normalized cumulative κ_l as a function of frequency is shown in the inset. Note the logarithmic scale.

the three-phonon anharmonic absorption and emission phase space, shown in Fig. 6. The scattering phase space is larger for the hexagonal structure than for the cubic one, reflecting differences in the phonon dispersions.

The phonon lifetimes, related to the third-order anharmonic IFCs, are also important. The anharmonic scattering rates at 300 K are presented in Fig. 7. As seen, the scattering rates of hexagonal KBaBi are larger than those of the cubic structure in the low-frequency regions (below 1 THz), but the anharmonic scattering rates for cubic KBaBi are higher in an intermediate-frequency range. This affects contributions of phonon modes to lattice thermal conductivity, as shown in the cumulative thermal conductivity in the inset of Fig. 7. The net result is that the thermal conductivity of the ground state hexagonal phase is reduced due to stronger scattering of heat-carrying acoustic phonons. This results from both the larger scattering phase space and the larger anharmonic couplings.

IV. ELECTRONIC STRUCTURE AND ELECTRICAL TRANSPORT

Electronic structures and electrical transport properties were obtained using the all-electron general potential linearized augmented plane-wave (LAPW) method [39], as implemented in the WIEN2K code [40]. Importantly, the present calculations are based on the the modified Becke-Johnson (MBJ) potential of Tran and Blaha [41]. This potential generally gives improved band gaps relative to experiment for most semiconductors compared to the standard PBE-GGA functional, particularly for compounds that do not include transition elements [41–44]. Spin-orbit coupling (SOC) was included for the electronic properties. We used a basis set cutoff parameter $R_{\min}K_{\max} = 9$, where $R_{\min}$ is the smallest sphere radius and $K_{\max}$ is the plane-wave cutoff. The electronic transport parameters were calculated using the BOLTZTRAP code [45]. These transport calculations were based on first-principles calculations on a **k**-point mesh with approximately 50 000 points in the irreducible Brillouin zone, with the needed relaxation time determined using deformation potential theory.

We focus on the hexagonal ground state structure. The band structure and corresponding DOS as obtained with the MBJ potential are shown in Figs. 8 and 9, respectively. Although it is composed of metallic elements, hexagonal KBaBi is predicted to be a semiconductor.

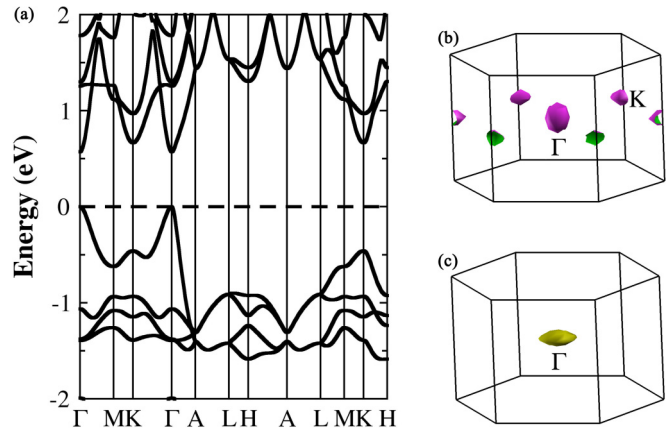

FIG. 8. (a) Band structure of hexagonal KBaBi as determined using the modified Becke-Johnson potential and carrier pocket shapes as given by isosurfaces (b) 0.1 eV above the conduction band for electrons and (c) 0.1 eV below the valence band maximum for holes.

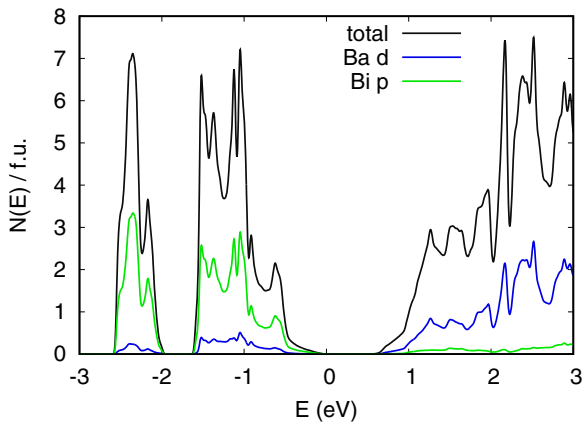

FIG. 9. Electronic density of states of hexagonal KBaBi and projections of Bi p and Ba d character. The projections are obtained as the weights inside LAPW spheres with a radius of 3.1 bohrs. This underestimates the contribution of extended orbitals that have substantial weight outside the sphere as is the case for the p orbital of the Bi anion. Spin-orbit coupling is included.

Previously, it was reported that KBaBi is a topological insulator due to a band inversion at the zone center. This report was based on a metallic scalar relativistic band structure that is then gapped by SOC, with a calculated band gap of 0.22 eV with the PBE-GGA [25]. It was also noted that the hybrid Heyd-Scuseria-Ernzerhof (HSE) functional gives a nontopological band structure for this compound [25]. Our PBE-GGA calculations reproduce the prior result of a metallic scalar relativistic band structure and a topological band structure including SOC (0.20 eV calculated gap). However, with the MBJ potential, we find a semiconducting band structure in a scalar relativistic approximation, which remains a trivial nontopological semiconductor with SOC. Specifically, the band structure remains noninverted, with band extrema remaining at the symmetry points. Since the MBJ potential is generally more reliable for the electronic structure of semiconductors, especially the band gap, we proceed to analyze the electronic properties based on the MBJ results. It should be noted that, usually, topological band structures are expected to be better for thermoelectric performance than nontopological band structures [46]. Nonetheless, we do find favorable electronic behavior that, combined with the very low lattice thermal conductivity, suggests potentially good thermoelectric performance.

The calculated band gap of 0.53 eV is in the range normally found in thermoelectric materials. The band gap is direct at Γ. The carrier pocket shapes are shown in Figs. 8(b) and 8(c). Interestingly, they have different anisotropies for the p type and n type. The holes have significantly heavier mass in the ab plane, as seen in the pancake shape, while the electrons are more nearly isotropic. At low carrier concentration, the calculated transport effective masses in units of the bare electron mass are $m_h^* = 0.86$ and $m_h^* = 0.17$ for holes in the in-plane and c-axis directions, respectively, and $m_e^* = 0.42$ and $m_e^* = 0.38$ for electrons in the in-plane and c-axis directions, respectively. Thus, the electrical conductivity has substantial anisotropy for the p type, which then leads to anisotropy in ZT, while as usual the Seebeck coefficient shows much lower anisotropy [47]. The much lower anisotropy of S compared to σ favors high ZT in the c-axis orientation for the p type. Also interestingly, there is a second set of carrier pockets near the K point of the zone, which comes from a secondary conduction band minimum, as seen in the band structure. This can favor high ZT for the n type.

The DOS shows a sharper onset for the conduction band than the valence band, although both the conduction and valence bands show an increasing mass with carrier concentration, as seen in the more rapid increase in the DOS as one moves away from the band edge. The valence band has primarily Bi p character, corresponding to the ionic picture discussed above in which Bi occurs as trivalent anions with nominally filled Bi p states. The conduction band is dominated by Ba d states. There is additionally some weak hybridization between the Bi p and Ba d states, as is evident from the Ba d contributions to the valence band seen in Fig. 9.

Calculation of the electrical transport properties within Boltzmann theory requires a scattering time τ, which is a function of both temperature and doping level. For this purpose we assume that acoustic phonon scattering dominates, as is typically the case for good thermoelectric materials. We calculate the temperature- and energy-dependent τ from deformation potential theory [48], with implementation as described in previous work [49]. The needed average longitudinal sound velocity was obtained by calculating the elastic constants from the stress-strain relationship, and the deformation potentials E_d for electrons and holes were obtained from the shifts of the conduction and valence band edges with changes in volume. The values of the deformation potentials are thus derived from shifts in the valence and conduction band edges with volume, which require a reference. The reference energy used here is the energy of the lowest calculated band, which is ∼28.4 eV below the valence band maximum, which results in deformation potentials of −4.90 eV and −6.93 eV for the conduction and valence bands. The effective masses are determined as the transport effective masses obtained from calculations using BOLTZTRAP. This procedure leads to somewhat lower deformation potentials than were recently reported by Barman and coworkers [27], presumably related to the choice of the reference level. Details of the band shifts for the deformation potential and the calculated relaxation time are given in the Supplemental Material [50].

As discussed above, band structure is important for thermoelectric performance because it is necessary to have band structures that can provide both high conductivity and a high Seebeck coefficient. The complex band shapes found in topological insulators provide one avenue for this. Other band features that can improve thermoelectric performance are band convergence, where multiple carrier pockets near the Fermi level contribute to transport, and carrier pocket anisotropy, where the different directional averages can lead to improved performance [51,52]. In the present case, the secondary pockets near the conduction band minimum are beneficial, as are the anisotropies of the valence band and conduction band carrier pockets at Γ.

Calculated transport properties are shown in Fig. 10 as functions of p-type and n-type doping levels at 1000 K. Transport properties at 300 K, where ZT is lower due to higher lattice thermal conductivity and lower Seebeck

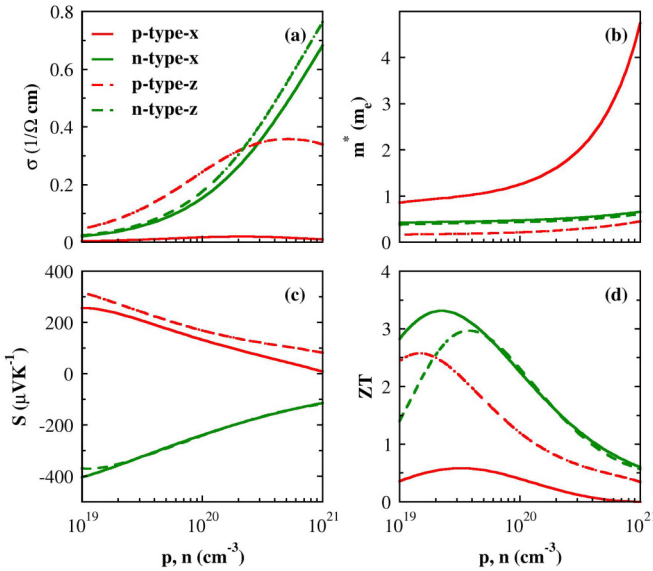

FIG. 10. Calculated transport properties of hexagonal KBaBi: (a) electrical conductivity, (b) transport effective mass for conductivity, (c) Seebeck coefficient, and (d) thermoelectric figure of merit. The values shown are at 1000 K. The plots are based on the anisotropic electrical properties. The thermal conductivity in ZT is from the calculated κ_l (see text) plus an electronic part, κ_e, based on the Wiedemann-Franz relation.

coefficient, are given in the Supplemental Material [50]. The transport effective mass shown is the value of the mass in a single parabolic band that would give the same conductivity as the actual band structure, with a fixed value of the relaxation time. The estimated ZT values are based on the electrical transport properties, a thermal conductivity that is the lattice thermal conductivity, as calculated above, and an electrical part from the Wiedemann-Franz relation. As seen, the direction-averaged effective mass is similar for the p type and n type. However, the magnitude of the Seebeck coefficient is higher for the n type at fixed carrier concentration. This shows that the band structure decoupling of S and σ is better in the conduction band overall. This leads to a higher power factor for a given carrier concentration and therefore a higher direction-averaged ZT for the n type.

The maximum ZT is estimated to be high, of the order of $ZT = 3$ for the n type, with high values in either the a-axis or c-axis direction. Similar values of ZT can also be obtained for the c-axis-oriented p type, while the values are significantly lower along the a axis for the p type. The high ZT values are predicted to occur at p-type and n-type doping levels of approximately 3×10^{19} and 5×10^{19} cm^{-3}. A main factor in these high values of ZT is the low lattice thermal conductivity.

V. SUMMARY AND CONCLUSIONS

We used global optimization crystal structure determination to identify the ground state structure of KBaBi. It is predicted to be a layered hexagonal structure. We found that the material is a semiconductor with a gap close to 0.5 eV, which is in the range typical of good thermoelectric materials. Although the basic bonding is ionic, there is significant hybridization between the Bi p orbitals that dominate the valence band and the Ba d states making up the conduction band. The result is dispersive bands with an effective mass of $\sim 0.5 m_e$ for both holes and electrons. The nature of the bonding with Zintl stabilized anionic BaBi sheets leads to a soft anharmonic lattice with exceptionally low thermal conductivity. The combination of low thermal conductivity and dispersive bands leads to the prediction of favorable thermoelectric performance. In contrast to prior reports based on the PBE-GGA, we find a topologically trivial semiconductor with a direct gap at Γ when the MBJ potential is used. This is a consequence of the noninverted band structure that is obtained, where the band extrema remain at the symmetry points with inclusion of SOC.

Solid-state compounds based on Bi^{3-} anions are relatively rare and have been little studied compared to solids containing Bi^{3+}, for example. Thus, the predicted stability of KBaBi as a semiconductor provides a unique opportunity to investigate the interplay of structure, bonding, and transport properties in a material with a rather distinct chemistry. Key questions for experiments to address include (1) the synthesis of the predicted phase, which is expected to be stable, (2) confirmation of its crystal structure, (3) spectroscopic measurements to determine the size of the band gap, (4) determination of whether the band structure is topological or trivial, and (5) whether the material can be doped and what the transport properties of the doped material are. We hope that the present work will motivate experimental effort to investigate this interesting phase.

ACKNOWLEDGMENTS

The work was supported by National Science Foundation of China, Awards No. 12047518, No. 11774347, and No. 11674083, and the China Postdoctoral Science Foundation (Grant No. 2020TQ0088).

[1] L. E. Bell, Science **321**, 1457 (2008).
[2] J. Yang and T. Caillat, MRS Bull. **31**, 224 (2006).
[3] M. W. Gaultois, T. D. Sparks, C. K. H. Borg, R. Seshadri, W. D. Bonificio, and D. R. Clarke, Chem. Mater. **25**, 2911 (2013).
[4] J. He and T. M. Tritt, Science **357**, eaak9997 (2017).
[5] J. Yang, L. Xi, W. Qiu, X. Shi, L. Chen, J. Yang, W. Zhang, C. Uher, and D. J. Singh, npj Comput. Mater. **2**, 15015 (2016).
[6] G. Xing, J. Sun, Y. Li, X. Fan, W. Zheng, and D. J. Singh, Phys. Rev. Mater. **1**, 065405 (2017).
[7] J. Recatala-Gomez, A. Suwardi, I. Nandhakumar, A. Abutaha, and K. Hippalgaonkar, ACS Appl. Energy Mater. **3**, 2240 (2020).
[8] C. Wood, Rep. Prog. Phys. **51**, 459 (1988).
[9] B. Poudel, Q. Hao, Y. Ma, Y. Lan, A. Minnich, B. Yu, X. Yan, D. Wang, A. Muto, D. Vashaee, X. Chen, J. Liu, M. S. Dresselhaus, G. Chen, and Z. Ren, Science **320**, 634 (2008).
[10] A. J. Minnich, M. S. Dresselhaus, Z. F. Ren, and G. Chen, Energy Environ. Sci. **2**, 466 (2009).

[11] Z. G. Chen, G. Han, L. Yang, L. Cheng, and J. Zou, Prog. Nat. Sci.: Mater. Int. **22**, 535 (2012).
[12] L. Lindsay, C. Hua, X. L. Ruan, and S. Lee, Mater. Today Phys. **7**, 106 (2018).
[13] T. Takabatake, K. Suekuni, T. Nakayama, and E. Kaneshita, Rev. Mod. Phys. **86**, 669 (2014).
[14] M. D. Nielsen, V. Ozolins, and J. P. Heremans, Energy Environ. Sci. **6**, 570 (2013).
[15] E. J. Skoug and D. T. Morelli, Phys. Rev. Lett. **107**, 235901 (2011).
[16] J. Carrete, W. Li, N. Mingo, S. Wang, and S. Curtarolo, Phys. Rev. X **4**, 011019 (2014).
[17] Z. Feng, Y. Fu, Y. Zhang, and D. J. Singh, Phys. Rev. B **101**, 064301 (2020).
[18] S. Chen and Z. Ren, Mater. Today **16**, 387 (2013).
[19] C. Fu, S. Bai, Y. Liu, Y. Tang, L. Chen, X. Zhao, and T. Zhu, Nat. Commun. **6**, 8144 (2015).
[20] Y. Xing, R. Liu, J. Liao, Q. Zhang, X. Xia, C. Wang, H. Huang, J. Chu, M. Gu, T. Zhu, C. Zhu, F. Xu, D. Yao, Y. Zeng, S. Bai, C. Uher, and L. Chen, Energy Environ. Sci. **12**, 3390 (2019).
[21] E. S. Toberer, A. F. May, C. J. Scanlon, and G. J. Snyder, J. Appl. Phys. **105**, 063701 (2009).
[22] F. Casper, R. Seshadri, and C. Felser, Phys. Status Solidi A **206**, 1090 (2009).
[23] W. Bażela and A. Szytula, Phys. Status Solidi A **66**, 45 (1981).
[24] H. Kleinke and H. Franzen, Z. Anorg. Allg. Chem. **624**, 51 (1998).
[25] X. Zhang, Q. Liu, Q. Xu, X. Dai, and A. Zunger, J. Am. Chem. Soc. **140**, 13687 (2018).
[26] Z. L. Lv, L. Zhao, Y. Wang, and H. Y. Wang, J. Solid State Chem. **276**, 272 (2019).
[27] N. Barman, A. Barman, and P. K. Haldar, J. Solid State Chem. **296**, 121961 (2021).
[28] Y. Wang, J. Lv, L. Zhu, and Y. Ma, Comput. Phys. Commun. **183**, 2063 (2012).
[29] Y. Wang, J. Lv, L. Zhu, and Y. Ma, Phys. Rev. B **82**, 094116 (2010).
[30] J. P. Perdew, K. Burke, and M. Ernzerhof, Phys. Rev. Lett. **77**, 3865 (1996).
[31] P. E. Blöchl, Phys. Rev. B **50**, 17953 (1994).
[32] G. Kresse and J. Furthmüller, Comput. Mater. Sci. **6**, 15 (1996).
[33] A. Savin, O. Jepsen, J. Flad, O. K. Andersen, H. Preuss, and H. G. von Schnering, Angew. Chem., Int. Ed. Engl. **31**, 187 (1992).
[34] A. Togo, F. Oba, and I. Tanaka, Phys. Rev. B **78**, 134106 (2008).
[35] W. Li, J. Carrete, N. A. Katcho, and N. Mingo, Comput. Phys. Commun. **185**, 1747 (2014).
[36] A. Ward, D. A. Broido, D. A. Stewart, and G. Deinzer, Phys. Rev. B **80**, 125203 (2009).
[37] W. Li, L. Lindsay, D. A. Broido, D. A. Stewart, and N. Mingo, Phys. Rev. B **86**, 174307 (2012).
[38] Y. Fu, D. J. Singh, W. Li, and L. Zhang, Phys. Rev. B **94**, 075122 (2016).
[39] D. J. Singh and L. Nordstrom, *Planewaves, Pseudopotentials, and the LAPW Method*, 2nd ed. (Springer, Berlin, 2006).
[40] K. Schwarz, P. Blaha, and G. K. H. Madsen, Comput. Phys. Commun. **147**, 71 (2002).
[41] F. Tran and P. Blaha, Phys. Rev. Lett. **102**, 226401 (2009).
[42] D. Koller, F. Tran, and P. Blaha, Phys. Rev. B **83**, 195134 (2011).
[43] D. J. Singh, Phys. Rev. B **82**, 205102 (2010).
[44] H. Jiang, J. Chem. Phys. **138**, 134115 (2013).
[45] G. K. H. Madsen and D. J. Singh, Comput. Phys. Commun. **175**, 67 (2006).
[46] H. Shi, D. Parker, M. H. Du, and D. J. Singh, Phys. Rev. Appl. **3**, 014004 (2015).
[47] K. P. Ong, D. J. Singh, and P. Wu, Phys. Rev. Lett. **104**, 176601 (2010).
[48] J. Bardeen and W. Shockley, Phys. Rev. **80**, 72 (1950).
[49] Z. Feng, Y. Fu, A. Putatunda, Y. Zhang, and D. J. Singh, Phys. Rev. B **100**, 085202 (2019).
[50] See Supplemental Material at http://link.aps.org/supplemental/10.1103/PhysRevB.103.224101 for details related to the deformation potential calculations and for 300 K transport data.
[51] D. Parker, X. Chen, and D. J. Singh, Phys. Rev. Lett. **110**, 146601 (2013).
[52] H. Shi, W. Ming, D. S. Parker, M.-H. Du, and D. J. Singh, Phys. Rev. B **95**, 195207 (2017).